AIAA SciTech Forum
6-10 January 2025, Orlando, FL
AIAA SCITECH 2025 Forum

10.2514/6.2025-2201

Characterizing Quasi-Secondary Instabilities in Compressible Flows Using the Structured Input-Output Framework

Diganta Bhattacharjee* and Maziar S. Hemati†
University of Minnesota, Minneapolis, MN 55455, USA

We extend the recently proposed structured input-output analysis framework to identify quasi-secondary instabilities in compressible flows. A key component of any structured input-output analysis is the uncertainty modeling, which arises due to a pseudo-linearization of the quadratic nonlinearity in the governing flow equations. The uncertainty element can be interpreted as a realization of a flow-field 'frozen' in time and the homogeneous spatial coordinates, which modifies elements of the base flow with which linear instabilities interact (i.e., quasi-secondary instabilities). We improve upon recently introduced methods for computing structured uncertainties that arise in the context of incompressible flows, focusing on straightforwardness and computational tractability. Results from our proposed analysis method qualitatively match prior results in the literature on incompressible Couette and channel flows. We then extend these methods for the analysis of compressible flows. Analysis of a compressible laminar Couette flow at subsonic, transonic, and supersonic conditions reveals that the spatial auto-correlation structures capture the Mach-number-dependence of the momentum and thermodynamic properties of a flow instability. For example, the specific volume auto-correlations amplify with an increase in the Mach number and thereby introduce a larger modification to the thermodynamic properties of the base flow. These findings are further corroborated by the structured forcing modes associated with the instability.

I. Introduction

An ability to identify and characterize instability mechanisms in compressible flows is key for aerospace applications. Model-based methods like input-output (I/O) or resolvent analysis have been successful in uncovering important flow physics in the incompressible regime [1–4] and are getting increasingly popular for analyzing compressible flows as well [5–12]. I/O methods are inherently physics-based and work by decomposing the governing flow equations into a feedback interconnection between the linear dynamics and the nonlinear terms. Traditionally, the outputs of the nonlinear terms are treated as an implicit (unstructured) forcing on the linear dynamics, which results in an optimization problem that is relatively straightforward to solve using linear systems analysis techniques.

The structured I/O analysis framework was proposed within the context of incompressible flows that imposes structural information of the quadratic convective nonlinearity, via a pseudo-linearization, within the linear I/O analysis framework [13]. The structured I/O analysis of incompressible flows in [13] led to results that were in agreement with both experimental observations and direct numerical simulation results. It was further shown in [14, 15] that additional repeated structure in the convective nonlinearity in the incompressible Navier-Stokes equations (NSE) can be exploited to further refine the structured I/O analysis. Moreover, the structured I/O framework can be utilized to conduct modal analysis, as shown in [16], and has been used to elucidate flow physics in stratified flow [17] and turbulent flows [15, 18]. It is noteworthy that the structured I/O modal analysis is able to capture nonlinear flow behaviors like the dampening of the near-wall cycle and creation of Kelvin-Helmholtz-type instabilities for turbulent flows over riblets that are consistent with direct numerical simulation results [18]. Recently, the structured I/O framework has been extended to be applicable for compressible flows [19, 20] and the associated uncertainty model is substantially more complicated than that in the incompressible flows.

While the structured I/O gain provides an estimate of the robust stability margin of the flow perturbations, the analysis also allows computation of structured uncertainties consistent with the structure of the nonlinearity. In the context of analyzing fluid flows, this uncertainty can be interpreted as a collection of time-invariant gains that describe

---

*Postdoctoral Research Associate, Department of Aerospace Engineering and Mechanics, AIAA Member. Email: dbhattac@umn.edu
†Associate Professor, Department of Aerospace Engineering and Mechanics, AIAA Associate Fellow. Email: mhemati@umn.edu

the spatial structures associated with the quantities modeled through the uncertainty. For example, in the case of incompressible flows, the structured uncertainty models the velocity field related to the convective nonlinearity in the incompressible NSE [14, 21], and the gains in that case represent spatial structures of the velocity field in the wall-normal coordinate [22]. These gains are also closely linked with 'optimal' perturbations responsible for maximum amplification of the flow perturbations [22]. We note here that the structured uncertainty can also be viewed as a 'frozen' flow-field, serving to modify the base flow upon which a linear stability analysis is conducted. This is akin to base flow modifications associated with primary instabilities used in secondary instability analysis for predicting transition to turbulence [23–26]. We utilize the term '*quasi-secondary*' instability in this paper to distinguish from the traditional secondary instabilities in the existing literature. In particular, the distinguishing factors here are essentially two-fold: (a) the structured uncertainty modifies a subset of base flow terms in the linear perturbation dynamics, thus leading to *quasi-base flow modifications* (see Section III); (b) the structured uncertainty does not explicitly depend on a primary source of instability and manifests itself through the pseudo-linearization of the nonlinearity in the governing flow equations.

In this paper, we provide an efficient method for computing the structured uncertainty, which can be studied to gain further insight into the flow physics. We first implement our method on incompressible Couette and channel flows to compute the structured uncertainty components associated with the largest flow amplification as indicated by the input-output gain. A similar component-wise analysis was conducted in [22], which involved a refinement of the uncertainty structure. While the standard structured uncertainty for an incompressible flow comprises three non-repeated complex full-blocks (see, e.g., [13]), the refinement in [22] led to a structured uncertainty with nine non-repeated blocks. Our results here demonstrate that the findings reported in [22] can be obtained using the standard uncertainty structure as well. The analysis in [22] as well as other prior work in the literature [13, 27] often implement the off-the-shelf 'mussv' package provided in MATLAB's Robust Control Toolbox [28] for the analysis. However, the package incurs significant computational overheads due to its generality; in our experience of working with mussv, computations do not generally scale well to problem sizes that are routinely encountered when analyzing compressible flows. In this paper, we illustrate that our current implementation, which is streamlined for uncertainty sets arising within the context of structured I/O, has the potential to alleviate the computational cost.

Next, we implement the method for a compressible, plane Couette flow at subsonic, transonic and supersonic Mach numbers. The flow features embedded within the structured uncertainty related to a potential source of instability, as indicated by the input-output gains, are investigated. The spatial (wall-normal coordinate) auto-correlations in all the flow states (specific volume, velocity components and pressure) are mostly concentrated near the upper wall at the subsonic Mach number but these shift more towards the channel center with an increase in the Mach number. Also, our results showcase that the spatial structures related to momentum characteristics of the instability are dominated by the spanwise and wall-normal velocity components across the range of Mach numbers considered here. The specific volume auto-correlations are found to be smaller at subsonic Mach numbers compared to the transonic and supersonic structures. The instability influences thermodynamic properties of the base flow more as the Mach number increases. An investigation into the structured forcing mode shapes associated with the instability reveals that the modal behavior further corroborates the above-mentioned thermodynamic characteristic. Therefore, the spatial auto-correlation structures are able to provide insight into the momentum and thermodynamic characteristics related to a source of instability in compressible flows.

The remainder of this paper is organized as follows: A summary of the structured I/O modeling and the current method of computing structured uncertainties is provided in Section II. The analysis and results corresponding to incompressible and compressible flows are discussed in Sections III and IV, respectively. Finally, the concluding remarks are provided in Section V.

II. Structured Uncertainty Modeling and Computation

Consider the incompressible or compressible NSE given by

$$\frac{\partial \tilde{q}}{\partial t} = \mathcal{N}(\tilde{q}), \tag{1}$$

where $\tilde{q}$ are the flow variables (with the notation $\tilde{(\cdot)}$ denoting the total field) chosen to describe the flow in a three-dimensional domain, and $\mathcal{N}(\cdot)$ denotes the nonlinearity in the governing equations. We are interested in the dynamics of the flow perturbations q about a steady (i.e., invariant with respect to time) base-flow profile q_0, both of which are related to the total field as $\tilde{q} = q + q_0$. To that end, the dynamics of perturbations—obtained by substituting $\tilde{q} = q + q_0$ into (1)—can be split into linear and nonlinear parts that are in feedback with each other and expressed as

$$\frac{\partial q}{\partial t} = \mathcal{L}q + \mathcal{F}(q), \tag{2}$$

where $\mathcal{L}$ is a linearization (i.e., the Jacobian) of the nonlinearity $\mathcal{N}(\cdot)$ evaluated at the base-flow profile q_0, and $\mathcal{F}(\cdot)$ contains all the remaining nonlinear terms (see Fig. 1a). Analyzing this nonlinear system poses nontrivial challenges and usually leads to computational intractability and other issues [21, 29–33]. Taking the resolvent analysis approach, one can replace the nonlinearity as some implicit forcing which removes the dependence of the nonlinearity on the flow variables. This is equivalent to removing the feedback interconnection between the linear and nonlinear parts of the governing flow system (compare the schematics in Fig. 1). As mentioned in the Introduction, Structured I/O analysis, on the other hand, proposes a pseudo-linear modeling of the above-mentioned nonlinearity and embeds the structural information of the nonlinearity into a structured uncertainty [13, 14, 20]. This modeling allows for structured singular value (or, simply 'μ')[34, 35]—a well-established concept from robust control theory—to be implemented for the subsequent analysis, which provides an estimate of the stability margin of the associated flow perturbations.

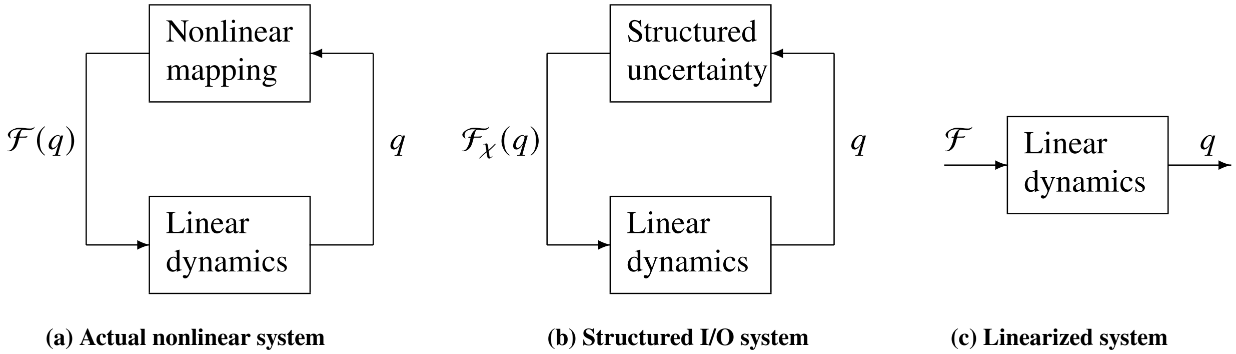

(a) Actual nonlinear system **(b) Structured I/O system** **(c) Linearized system**

Fig. 1 Stability of transitional fluid flows and the governing equations of perturbations (q) about a steady base flow. These equations are shown in three different forms: (a) the original system with the linear dynamics in feedback with the nonlinearity $\mathcal{F}(q)$); (b) the structured I/O modeling with $\mathcal{F}_\chi(q)$) representing the approximated nonlinearity [20]; (c) the linearized system, typically used for resolvent analysis, obtained by removing the aforementioned feedback connection.

We will assume that the base-flow is homogeneous in the streamwise and spanwise spatial coordinates as well as in time, and it is inhomogeneous in the wall-normal coordinate/direction. Thus, we utilize Fourier bases for time (i.e., harmonic time-dependence) and the homogeneous spatial coordinates and a Chebyshev polynomial basis for the inhomogeneous coordinate. After discretization, the equations governing the structured I/O system can be summarized as [13, 14, 20]

$$\begin{aligned} \mathbf{i}\omega\mathbf{q} &= \mathbf{L}(k_x, k_z)\mathbf{q} + \mathbf{B}_\chi\mathbf{f}_\chi \\ \mathbf{y}_\chi &= \mathbf{C}_\chi(k_x, k_z)\mathbf{q} \\ \mathbf{f}_\chi &= \operatorname{diag}\left(\Delta_1, \Delta_2, \ldots, \Delta_{N_\Delta}\right)\mathbf{y}_\chi = \Delta\mathbf{y}_\chi \end{aligned} \tag{3}$$

where $\mathbf{i} = \sqrt{-1}$ stands for the imaginary unit, ω is the temporal frequency, k_x and k_z are respectively the streamwise and spanwise wavenumbers, and all the quantities with a subscript $(\cdot)_\chi$ are obtained through the structured I/O modeling. Here, $\mathbf{L}(k_x, k_z)$ and $\mathbf{C}_\chi(k_x, k_z)$ are the discretized operators. Note that the structured uncertainty Δ takes specific block-diagonal structures for incompressible and compressible flows, but essentially contains complex matrices in both cases typically referred to as 'complex full-blocks' and we will consider the non-repeated case, i.e., $\Delta_i \neq \Delta_j$, to simplify the analysis. We will outline a computationally efficient framework for computing such Δs in this section. The system of equations in (3) can be interpreted as a feedback interconnection between a linear time-invariant (LTI) system and a structured uncertainty Δ. In this interpretation, the inputs to and outputs from the LTI system are $\mathbf{f}_\chi \in \mathbb{C}^{n_f}$ and $\mathbf{y}_\chi \in \mathbb{C}^{n_y}$, respectively. Furthermore, the I/O relationship can be written as

$$\mathbf{y}_\chi = \mathbf{H}(k_x, k_z, \omega)\mathbf{f}_\chi \tag{4}$$

where $\mathbf{H}(k_x, k_z, \omega) = \mathbf{C}_\chi(k_x, k_z)(\mathbf{i}\omega\mathbf{I}_{n_q} - \mathbf{L}(k_x, k_z))^{-1}\mathbf{B}_\chi$ is the spatio-temporal frequency response operator that maps the modeled inputs $\mathbf{f}_\chi$ to the corresponding modeled outputs $\mathbf{y}_\chi$ at a given tuple (k_x, k_z, ω). Here, $\mathbf{I}_n$ is the $n \times n$ identity matrix and n_q is the dimension of the discretized flow state $\mathbf{q}$ that depends on the number of collocation points in the wall-normal direction.

As stated above, the structured I/O analysis utilizes the concept of structured singular value or μ. However, note that exactly computing μ is NP-hard for a general uncertainty structure [36–38]. Thus, it is a common practice to compute upper and lower bounds on μ instead. We will start the discussion here by recalling the definition of μ for a given matrix $\mathbf{H} \in \mathbb{C}^{n\times m}$ and a set of structured uncertainties comprising N_Δ non-repeated complex full-blocks as

$$\mathbf{\Delta}_{F_{N_\Delta}} = \{\text{diag}\left(\Delta_1, \Delta_2, \ldots, \Delta_{N_\Delta}\right) : \Delta_i \in \mathbb{C}^{m_i\times n_i}\} \subset \mathbb{C}^{m\times n}. \tag{5}$$

Note that the structured uncertainty in (3) belongs to this set and we will use the term 'non-repeated full-block' in this paper to describe this structured uncertainty set.

Definition 1 ([34, 35]) *For a given matrix* $\mathbf{H} \in \mathbb{C}^{n\times m}$ *and a set of structured matrices* $\mathbf{\Delta}_{F_{N_\Delta}} \subset \mathbb{C}^{m\times n}$*, the structured singular value is defined as*

$$\mu_{\mathbf{\Delta}_F}(\mathbf{H}) = \frac{1}{\min(\|\Delta\|_2 : \Delta \in \mathbf{\Delta}_{F_{N_\Delta}}, \det(\mathbf{I}_n - \mathbf{H}\Delta) = 0)} \tag{6}$$

where $\|\cdot\|_2$ *denotes the spectral norm of a matrix. If there does not exist* $\Delta \in \mathbf{\Delta}_{F_{N_\Delta}}$ *such that* $\det(\mathbf{I}_n - \mathbf{H}\Delta) = 0$*, then* $\mu_{\mathbf{\Delta}_{F_{N_\Delta}}}(\mathbf{H}) = 0$.

Note that $\mu_{\mathbf{\Delta}_F}(\mathbf{H})$ depends both on the matrix $\mathbf{H}$ and the set $\mathbf{\Delta}_{F_{N_\Delta}}$; however, we will drop the subscript when the uncertainty set is obvious from the context of the discussion. Next, we will briefly summarize the procedure for computing a $\Delta \in \mathbf{\Delta}_{F_{N_\Delta}}$ as well as the associated lower bound on μ. To that end, we implement the power iteration method (or, simply the power method) for complex uncertainties in [34, 39], which is an efficient method to find uncertainties $\Delta \in \mathbf{\Delta}_{F_{N_\Delta}}$ that satisfy the determinant condition in Definition 1. Note that any particular $\Delta \in \mathbf{\Delta}_{F_{N_\Delta}}$ such that $\det(\mathbf{I}_n - \mathbf{H}\Delta) = 0$ yields a lower bound $\mu(\mathbf{H}) \geq \frac{1}{\|\Delta\|_2}$. The exact value of $\mu(\mathbf{H})$ corresponds to the "smallest" $\Delta \in \mathbf{\Delta}_{F_{N_\Delta}}$ (as measured in the spectral norm) such that $\det(\mathbf{I}_n - \mathbf{H}\Delta) = 0$ (see Definition 1). The determinant condition is equivalent to finding $\Delta \in \mathbf{\Delta}_{F_{N_\Delta}}$ and non-zero vectors $\mathbf{p} \in \mathbb{C}^n$ and $\mathbf{q} \in \mathbb{C}^m$ such that $\mathbf{p} = \mathbf{H}\mathbf{q}$ and $\mathbf{q} = \Delta\mathbf{p}$, and the power iteration computes these quantities by exploring optimality conditions associated with μ [39]. Thus, the power iteration computes complex-valued vectors $\mathbf{p}$ and $\mathbf{q}$ that are consistent with the input-output relationships of the feedback interconnection, meaning that these vectors abide by the structural constraints originating from the uncertainty—an aspect not captured in traditional resolvent-based modal analysis of fluid flows (see, for example, [6]). Therefore, power iteration provides a pathway for structured modal analysis. For example, Refs. [16, 18] describe such modal analysis of incompressible channel flows and turbulent flows over riblets. Moreover, the particular uncertainty Δ returned by the power iteration can be studied further for insight into the flow physics, which is the main objective of the current study.

Consider a given matrix $\mathbf{H} \in \mathbb{C}^{n\times m}$ and a set of structured uncertainties with two non-repeated full blocks as

$$\mathbf{\Delta}_{F_2} = \{\text{diag}(\Delta_1, \Delta_2) : \Delta_1 \in \mathbb{C}^{m_1\times n_1}, \Delta_2 \in \mathbb{C}^{m_2\times n_2}\} \tag{7}$$

where $m_1 + m_2 = m$ and $n_1 + n_2 = n$ for consistent dimensions. We will describe the power iteration for $\mathbf{\Delta}_{F_2}$, which can be generalized to any number of full-blocks as in (5) by simply duplicating the formulae provided here. The power iteration is described in terms of vectors $\mathbf{a}, \mathbf{z} \in \mathbb{C}^n$ and $\mathbf{b}, \mathbf{w} \in \mathbb{C}^m$. Now, these vectors are partitioned according to the dimensions of the full-blocks as

$$\mathbf{a} = \begin{bmatrix}\mathbf{a}_1\\ \mathbf{a}_2\end{bmatrix},\ \mathbf{z} = \begin{bmatrix}\mathbf{z}_1\\ \mathbf{z}_2\end{bmatrix},\ \mathbf{b} = \begin{bmatrix}\mathbf{b}_1\\ \mathbf{b}_2\end{bmatrix},\ \mathbf{w} = \begin{bmatrix}\mathbf{w}_1\\ \mathbf{w}_2\end{bmatrix},$$

Algorithm 1 Lower Bound: Power Iteration and Δ Computation

```
(Initialization) Choose the maximum number of iterations $\kappa_m$ and set $\kappa = 0$. Select $\mathbf{b}^{[0]}, \mathbf{w}^{[0]} \in \mathbb{C}^m$ as some unit-norm vectors, and set $\mathbf{a}^{[0]} = \mathbf{z}^{[0]} = 0 \in \mathbb{C}^n$.
while $\kappa < \kappa_m$ do
    (8a): $\beta := \|\mathbf{H}\mathbf{b}^{[\kappa]}\|_2$ and $\mathbf{a}^{[\kappa+1]} := \mathbf{H}\mathbf{b}^{[\kappa]}/\beta$.
    (8b): Use $(\mathbf{a}^{[\kappa+1]}, \mathbf{w}^{[\kappa]})$ to compute $\mathbf{z}^{[\kappa+1]}$.
    (8c): $\beta := \|\mathbf{H}^{\dagger}\mathbf{z}^{[\kappa+1]}\|_2$ and $\mathbf{w}^{[\kappa+1]} := \mathbf{H}^{\dagger}\mathbf{z}^{[\kappa+1]}/\beta$.
    (8d): Use $(\mathbf{a}^{[\kappa+1]}, \mathbf{w}^{[\kappa+1]})$ to compute $\mathbf{b}^{[\kappa+1]}$.
    Set $\kappa = \kappa + 1$.
end while
Take $\mathbf{a}^{[\kappa_m]}$, $\mathbf{b}^{[\kappa_m]}$ and $\beta$, and set $\mathbf{a} = \mathbf{a}^{[\kappa_m]}$ and $\mathbf{b} = \mathbf{a}^{[\kappa_m]}$.
Partition $\mathbf{a}$ and $\mathbf{b}$ into $\mathbf{a}_i$ and $\mathbf{b}_i$ according to the dimensions of full-blocks $\Delta_i$.
Set $\Delta_i^{[\mathrm{PI}]} = \frac{\mathbf{b}_i(\mathbf{a}_i)^{\dagger}}{\|\mathbf{a}_i\|^2}, i = 1, 2, \ldots, N_{\Delta}$.
(Output) Set $\mathbf{p} = \beta\mathbf{a}$, $\mathbf{q} = \mathbf{b}$, and $\Delta = \frac{1}{\beta}\mathrm{diag}\left(\Delta_1^{[\mathrm{PI}]}, \Delta_2^{[\mathrm{PI}]}, \ldots, \Delta_{N_\Delta}^{[\mathrm{PI}]}\right)$.
```

where $\mathbf{a}_1 \in \mathbb{C}^{n_1}$, $\mathbf{a}_2 \in \mathbb{C}^{n_2}$, $\mathbf{b}_1 \in \mathbb{C}^{m_1}$, $\mathbf{b}_2 \in \mathbb{C}^{m_2}$. The power iteration is then defined based on the following set of equations for some $\beta > 0$:

$$\beta\mathbf{a} = \mathbf{H}\mathbf{b} \tag{8a}$$

$$\mathbf{z}_1 = \frac{\|\mathbf{w}_1\|_2}{\|\mathbf{a}_1\|_2}\mathbf{a}_1, \ \ \mathbf{z}_2 = \frac{\|\mathbf{w}_2\|_2}{\|\mathbf{a}_2\|_2}\mathbf{a}_2 \tag{8b}$$

$$\beta\mathbf{w} = \mathbf{H}^{\dagger}\mathbf{z} \tag{8c}$$

$$\mathbf{b}_1 = \frac{\|\mathbf{a}_1\|_2}{\|\mathbf{w}_1\|_2}\mathbf{w}_1, \ \ \mathbf{b}_2 = \frac{\|\mathbf{a}_2\|_2}{\|\mathbf{w}_2\|_2}\mathbf{w}_2, \tag{8d}$$

where $(\cdot)^{\dagger}$ denotes the conjugate transpose and $\mathbf{a}$ and $\mathbf{w}$ are unit norm. The details for the derivation of these equations can be found in [34, 39]. Note that (8d) always implies $\|\mathbf{b}_1\|_2 = \|\mathbf{a}_1\|_2$ and $\|\mathbf{b}_2\|_2 = \|\mathbf{a}_2\|_2$. Hence, there are matrices $\mathbf{Q}_i \in \mathbb{C}^{m_i \times n_i}$ with $\|\mathbf{Q}_i\|_2 = 1, i = 1, 2$ such that $\mathbf{b}_i = \mathbf{Q}_i\mathbf{a}_i, i = 1, 2$. Finally, define the following

$$\mathbf{q} := \mathbf{b}, \quad \mathbf{p} := \beta\mathbf{a}, \quad \Delta := \frac{1}{\beta}\mathrm{diag}(\mathbf{Q}_1, \, \mathbf{Q}_2). \tag{9}$$

It can be verified from (8a) that $\mathbf{p} = \mathbf{H}\mathbf{q}$. Moreover, by construction, we have $\mathbf{q} = \Delta\mathbf{p}$ and $\|\Delta\|_2 = \frac{1}{\beta}$. Therefore, $\Delta \in \mathbf{\Delta}_{F_2}$ satisfies the determinant condition and yields the lower bound $\mu(\mathbf{H}) \geq \frac{1}{\|\Delta\|_2} = \beta$.

The power iteration is summarized in Algorithm 1, which works by iterating through the expressions in (8). For simplicity of presentation here, the algorithm is stated for a fixed number of iterations κ_m, but more sophisticated stopping criteria (e.g., terminating when the various vectors have small updates as measured in the Euclidean norm) can be easily incorporated as needed. The iterations for the vectors $\mathbf{b}^{[\kappa]}, \mathbf{w}^{[\kappa]}$ can be initialized with some unit-norm random vectors in $\mathbb{C}^m$. However, as suggested in [39], the initial values $\mathbf{b}^{[0]}, \mathbf{w}^{[0]}$ can be specifically chosen as the right singular vector associated with the largest singular value of $\mathbf{D}_1^{\star}\mathbf{H}\left(\mathbf{D}_2^{\star}\right)^{-1}$, where $\mathbf{D}_1^{\star}$, $\mathbf{D}_2^{\star}$ are matrices associated with the upper bound on μ and obtained using the Osborne's iteration (see, e.g., Section 3.1 in [14] for details). Note that this initialization works well in practice and we utilize it for all the numerical results included here.

III. Analysis of Incompressible Flows

In this section, we describe the quasi-base flow modification that manifests from the structured I/O modeling of the convective nonlinearity in the incompressible NSE. The incompressible NSE are given by

$$\frac{\partial\underline{\tilde{u}}}{\partial t} = \frac{1}{Re}\nabla^2\underline{\tilde{u}} - \nabla\tilde{p} - \underline{\tilde{u}} \cdot \nabla\underline{\tilde{u}} \tag{10}$$

with the associated zero divergence condition $\nabla \cdot \underline{\tilde{u}} = 0$. Here, $\underline{\tilde{u}}$ and $\tilde{p}$ denote the total velocity and pressure fields, respectively. The time is denoted using t and Re stands for the Reynolds number. Decomposing the total field into steady base flow and associated perturbation components, we have $\underline{\tilde{u}} = \underline{u} + \underline{u}_0$ and $\tilde{p} = p + p_0$. Therefore, the dynamics of the perturbations are governed by

$$\frac{\partial \underline{u}}{\partial t} = \frac{1}{Re}\nabla^2 \underline{u} - \nabla p - \underline{u}_0 \cdot \nabla \underline{u} - \underline{u} \cdot \nabla \underline{u}_0 - \underline{u} \cdot \nabla \underline{u}. \tag{11}$$

Now, the structured I/O modeling typically introduces the following pseudo-linearization [13, 18, 22] of the quadratic nonlinearity in (11):

$$\underline{u} \cdot \nabla \underline{u} \approx \underline{u}_\chi \cdot \nabla \underline{u} \tag{12}$$

where $\underline{u}_\chi$ denote the modeled terms. Thus, with this approximation, the nonlinear perturbation dynamics (11) becomes linear and are given by

$$\frac{\partial \underline{u}}{\partial t} = \frac{1}{Re}\nabla^2 \underline{u} - \nabla p - (\underline{u}_0 + \underline{u}_\chi) \cdot \nabla \underline{u} - \underline{u} \cdot \nabla \underline{u}_0. \tag{13}$$

Clearly, the modeled term only influences one of the two terms that are functions of the base flow $\underline{u}_0$. This serves as the primary reason for using phrases like 'quasi-secondary instability' or 'quasi-base flow modification' in this paper.

Next, we showcase our results for incompressible Couette and channel flows. The set of structured uncertainties for incompressible flows takes the following form:

$$\mathbf{\Delta}_{F_3} = \mathrm{diag}\,(\Delta_1, \Delta_2, \Delta_3) \tag{14}$$

where each block can be further decomposed as $\Delta_i = -\mathbf{u}_{\chi i}^\dagger = \begin{bmatrix} -u_{\chi i}^\dagger & -v_{\chi i}^\dagger & -w_{\chi i}^\dagger \end{bmatrix}, i = 1, 2, 3$. Here, $u_{\chi i}, v_{\chi i}, w_{\chi i} \in \mathbb{C}^{N_y \times N_y}$ where N_y stands for the number of collocation points in the wall-normal direction. Note that the above structure of the uncertainty is the one typically utilized in structured I/O analysis of incompressible flows (see, e.g., [13, 14, 17, 18]), but it is different from the one utilized in [22]. The uncertainty in [22] can be interpreted as an 'unrolled' version of the block-structure in (14) where all the sub-blocks in $\mathbf{u}_{\chi i}^\dagger$ (which are distributed along a row in (14)) are placed on the principal diagonal of the structured uncertainty (compare (14) with Eq. (12) in [22]). In this section, we show that we are able to generate results qualitatively similar to the ones reported in [22], despite working with the structured uncertainties as in (14). Each full-block Δ_i in (14) essentially maps the velocity gradients (which are the outputs here, $\mathbf{y}_\chi = \begin{bmatrix} (\nabla u)^\dagger & (\nabla v)^\dagger & (\nabla w)^\dagger \end{bmatrix}^\dagger$) in each of the spatial coordinates to the corresponding forcing for the momentum equation in that coordinate. Thus, in order to capture the relative contribution of each Δ_i, we can utilize

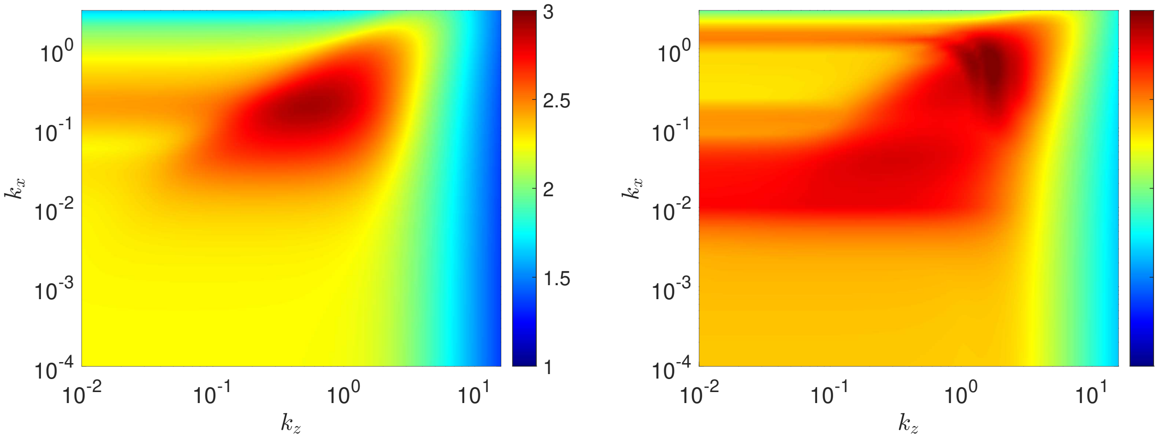

(a) Couette Flow at $Re = 358$

(b) Channel Flow at $Re = 690$

Fig. 2 The log-scaled upper bounds $\alpha_\mu\,(\mathbf{H}(k_x, k_z))$**. The maximum upper bound occurs at (a)** $(k_x, k_z, \omega) = (0.196, 0.578, 0)$**; (b)** $(k_x, k_z, \omega) = (0.692, 1.695, -0.383)$**.**

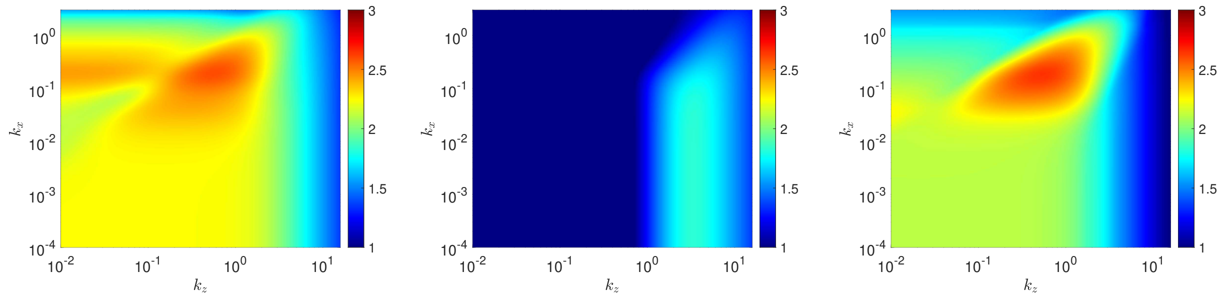

(a) $\log_{10}\left(\alpha_\mu(\mathbf{H}_1(k_x,k_z))\right)$ **(b)** $\log_{10}\left(\alpha_\mu(\mathbf{H}_2(k_x,k_z))\right)$ **(c)** $\log_{10}\left(\alpha_\mu(\mathbf{H}_3(k_x,k_z))\right)$

Fig. 3 The log-scaled μ upper bounds of $\alpha_\mu(\mathbf{H}_i(k_x,k_z))$ for the Couette flow at $Re = 358$.

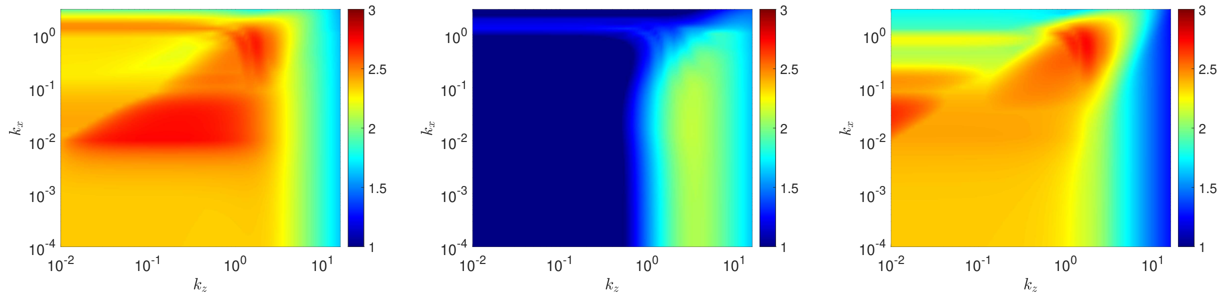

(a) $\log_{10}\left(\alpha_\mu(\mathbf{H}_1(k_x,k_z))\right)$ **(b)** $\log_{10}\left(\alpha_\mu(\mathbf{H}_2(k_x,k_z))\right)$ **(c)** $\log_{10}\left(\alpha_\mu(\mathbf{H}_3(k_x,k_z))\right)$

Fig. 4 The log-scaled μ upper bounds $\alpha_\mu(\mathbf{H}_i(k_x,k_z))$ for the channel flow at $Re = 690$.

the following frequency response operators:

$$\mathbf{H}_1(k_x,k_z,\omega) = \operatorname{diag}\left(\mathbf{I}_{3N_y},\mathbf{O}_{3N_y},\mathbf{O}_{3N_y}\right)\mathbf{H}(k_x,k_z,\omega) \tag{15}$$

$$\mathbf{H}_2(k_x,k_z,\omega) = \operatorname{diag}\left(\mathbf{O}_{3N_y},\mathbf{I}_{3N_y},\mathbf{O}_{3N_y}\right)\mathbf{H}(k_x,k_z,\omega) \tag{16}$$

$$\mathbf{H}_3(k_x,k_z,\omega) = \operatorname{diag}\left(\mathbf{O}_{3N_y},\mathbf{O}_{3N_y},\mathbf{I}_{3N_y},\right)\mathbf{H}(k_x,k_z,\omega) \tag{17}$$

where, for example, $\mathbf{H}_1(k_x,k_z,\omega)$ corresponds to the case where only Δ_1 is active (i.e., non-zero) and Δ_2, Δ_3 are identically zero. Therefore, for each $i, i = 1,2,3$, this is equivalent to setting the $\Delta_j = 0$ for all $j \neq i$, which is similar to the strategy utilized in [22]. In particular, we analyze the following incompressible flows: (a) plane Couette flow at $Re = 358$; (b) channel flow at $Re = 690$. Here, we will present numerical results for both the flows by considering a $n_{k_x} \times n_{k_z} \times n_\omega$ grid, where $n_{k_x}, n_{k_z}, n_\omega$ are the total number of grid points for k_x, k_z, and ω, respectively. We choose $(n_{k_x}, n_{k_z}) = (50, 90)$ logarithmically spaced points for the spatial wavenumbers in the range $k_x \in [10^{-4}, 10^{0.48}]$ and $k_z \in [10^{-2}, 10^{1.2}]$, and take $n_\omega = 50$ logarithmically spaced points for the temporal frequency in the range $\omega \in [-1, 1]$. Note that the computations were performed on a desktop computer with 3.61 GHz 12-th Gen Intel(R) Core(TM) i7-12700K processor with 12 cores and 16 GB RAM, and the results were generated using MATLAB R2022a.

The structured I/O gains (i.e., upper bounds on μ) for both the flows are shown in Fig. 2 where the upper bounds, denoted by $\alpha_\mu(\mathbf{H}(k_x,k_z))$, are chosen as the maximum of the upper bounds computed—using the Osborne's iteration [14, Section 3.1]—over the grid of temporal frequencies ω. Note that the results in Fig. 2 correspond to the operator $\mathbf{H}(k_x,k_z,\omega)$ and therefore correspond to the case where all the $\Delta_i, i = 1,2,3$, are active. On the other hand, the μ upper bound results pertaining to the relative contribution are shown in Figs. 3, 4, for which we have utilize the same (k_x,k_z,ω) grid as for the results in Fig. 2. The results in Fig. 3 indicate that the operator $\mathbf{H}_1(k_x,k_z,\omega)$ and the corresponding structured input-output gains are most closely associated with the overall system behavior. In the case of the channel flow, however, the results in Fig. 4 illustrate that both $\mathbf{H}_1(k_x,k_z,\omega)$ and $\mathbf{H}_3(k_x,k_z,\omega)$ predict similar input-output behavior as the overall system, with the upper bounds corresponding to $\mathbf{H}_1(k_x, k_z, \omega)$ matching more closely with the overall system behavior (compare Figs. 2b and 4a). These conclusions about the overall system and subsystem behavior are the same as in Section IV in [22].

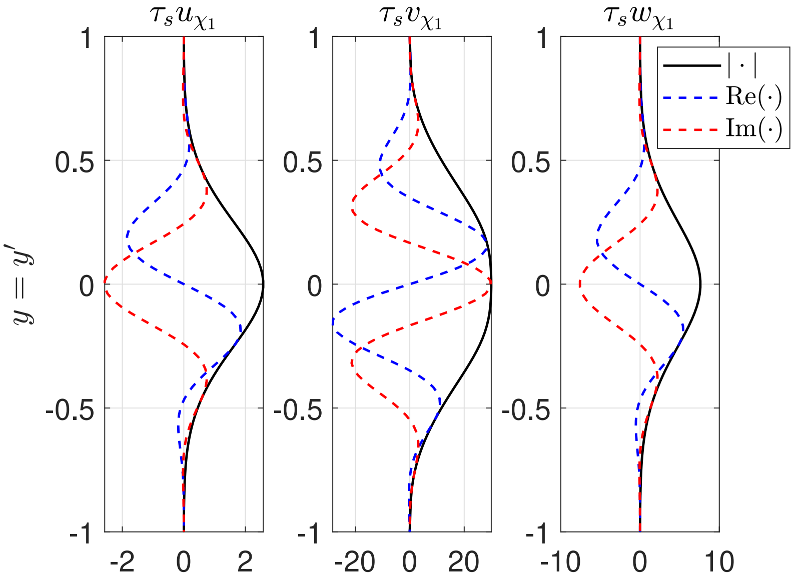

Fig. 5 The auto-correlation in the velocity components as captured via the structured uncertainty $\Delta_1 = \begin{bmatrix} -u_{\chi 1}^\dagger & -v_{\chi 1}^\dagger & -w_{\chi 1}^\dagger \end{bmatrix}$ for the Couette flow at $Re = 358$ and $(k_x, k_z, \omega) = (0.196, 0.578, 0)$. The parameter τ_s serves as a scaling factor for the purposes of illustration and here we have $\tau_s = 10^6$. Also, note that for $c \in \mathbb{C}$, $|c|$, $\mathrm{Re}(c)$, and $\mathrm{Im}(c)$ respectively denote the absolute value, the real part and the imaginary part of c.

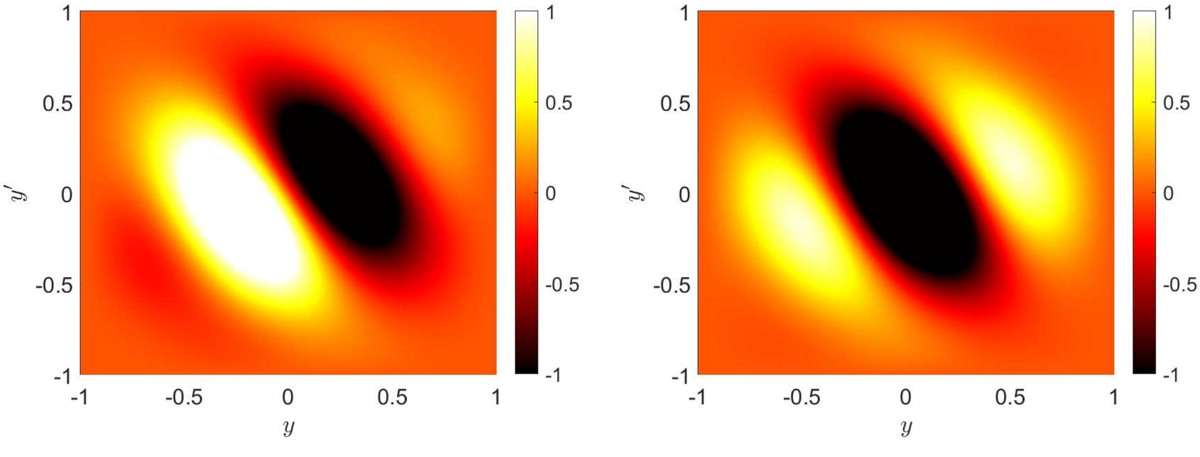

(a) $\mathrm{Re}\left(\tau_s u_{\chi 1}\right)$ **(b)** $\mathrm{Im}\left(\tau_s u_{\chi 1}\right)$

Fig. 6 The real and imaginary parts of the uncertainty associated with the Couette flow at $Re = 358$ and $(k_x, k_z, \omega) = (0.196, 0.578, 0)$. The parameter τ_s serves as a scaling factor for the purposes of illustration and here we have $\tau_s = 10^6$. Also, note that for $c \in \mathbb{C}$, $\mathrm{Re}(c)$ and $\mathrm{Im}(c)$ respectively denote the real and the imaginary parts of c.

Thus, to be consistent with the analysis in [22], we will focus on the uncertainty Δ_1 whose sub-blocks

$(-u^{\dagger}_{\chi_1}, -v^{\dagger}_{\chi_1}, -w^{\dagger}_{\chi_1})$ represent the correlations in the wall-normal coordinate for the three velocity components. We will use y, y' to denote the wall-normal coordinates (same as in [22]). The maximum amplification in the Couette flow perturbations at $Re = 358$ is for $(k_x, k_z, \omega) = (0.196, 0.578, 0)$, and we compute the associated $\Delta \in \mathbf{\Delta}_{F_3}$ by implementing the power iteration in Algorithm 1 on $\mathbf{H}(k_x, k_z, \omega)$ at this (k_x, k_z, ω) tuple. Figure 5 illustrates the real, imaginary and absolute values of the entries along the principal diagonals of the uncertainties u_{χ_1}, v_{χ_1}, and w_{χ_1}, which signify the auto-correlation in the respective velocity components at the same wall-normal location $y = y'$ [22]. We notice that the velocity components attain their peak magnitude and the real parts reverse sign—both at or near the channel. These not only qualitatively match the results reported in [22] but also are consistent with the observations from nonlinear optimal perturbation (NLOP) analysis in the literature. The (scaled) real and imaginary parts of u_{χ_1} are shown in Fig. 6, which indicate a peak near the channel center, given by $y = y' \approx 0$, as well as the real part switching sign near the channel center. Again, these are consistent with the observations in [22] and the actual flow physics.

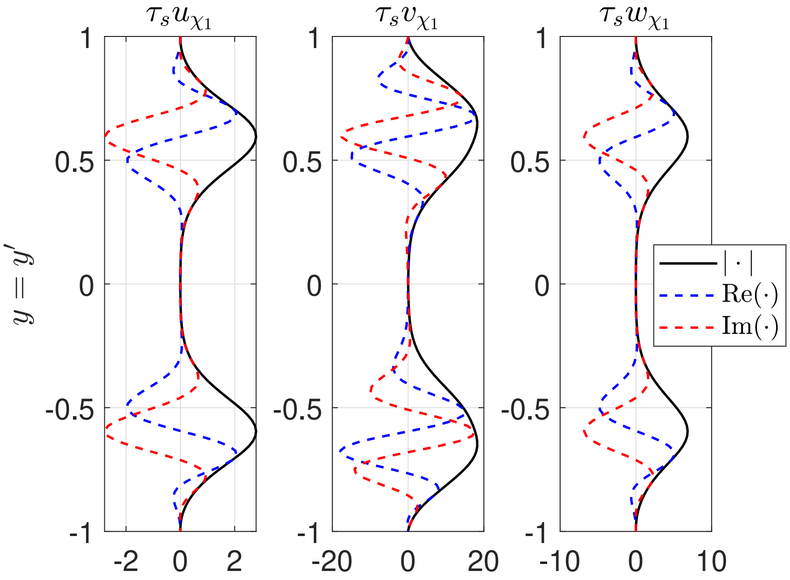

Fig. 7 The auto-correlation in the velocity components as captured via the structured uncertainty $\Delta_1 = \left[-u^{\dagger}_{\chi_1} \quad -v^{\dagger}_{\chi_1} \quad -w^{\dagger}_{\chi_1}\right]$ for the channel flow at $Re = 690$ and $(k_x, k_z, \omega) = (0.692, 1.695, -0.383)$. The parameter τ_s serves as a scaling factor for the purposes of illustration and here we have $\tau_s = 10^6$. Also, note that for $c \in \mathbb{C}$, $|c|$, $\mathrm{Re}(c)$, and $\mathrm{Im}(c)$ respectively denote the absolute value, the real part and the imaginary part of c.

For the channel flow, the velocity auto-correlations are as illustrated in Fig. 7 and the real and imaginary parts of the uncertainty u_{χ_1} are as shown in Fig. 8. These are again consistent with the results in [22]. Therefore, we have been able to capture the key results pertaining to incompressible flows without modifying the uncertainty modeling or the feedback interconnection as done in [22].

A comparison of the computation times between Algorithm 1 and mussv is shown in Fig. 9, where the computation times are plotted against the number of wall-normal collocation/grid points. It should be noted here that mussv is executed with the 'Uf' option to reduce the associated computational load. The higher computation times for mussv can be attributed towards the computational overheads within the package. Our implementation of Algorithm 1 does not inherit these overheads and results in a smaller computation time. Next, we have included the results and discussion for a compressible, laminar Couette flow.

IV. Compressible Flow Analysis: Plane, Compressible Couette Flow

The structured uncertainty in compressible flows contains non-repeated full-blocks corresponding to the velocity components ($\mathbf{u}_{\chi_i}$) as well as full-blocks that model the specific volume and pressure, which are denoted using ξ_{χ} and p_{χ},

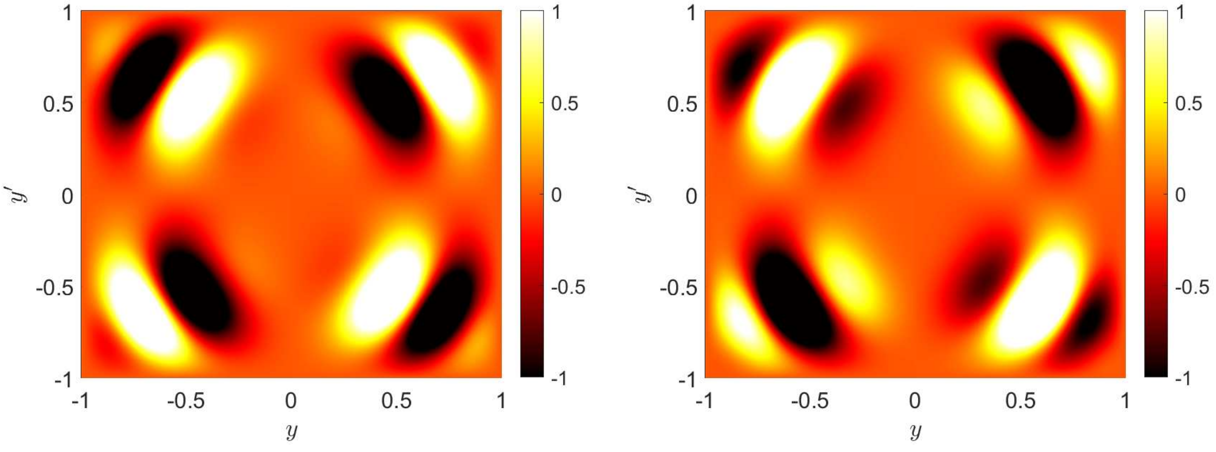

(a) $\mathrm{Re}\left(\tau_s u_{\chi 1}\right)$ **(b)** $\mathrm{Im}\left(\tau_s u_{\chi 1}\right)$

Fig. 8 The real and imaginary parts of the uncertainty associated with the channel flow at $Re = 690$ and $(k_x, k_z, \omega) = (0.692, 1.695, -0.383)$. The parameter τ_s serves as a scaling factor for the purposes of illustration and here we have $\tau_s = 10^6$. Also, note that for $c \in \mathbb{C}$, $\mathrm{Re}(c)$ and $\mathrm{Im}(c)$ respectively denote the real and the imaginary parts of c.

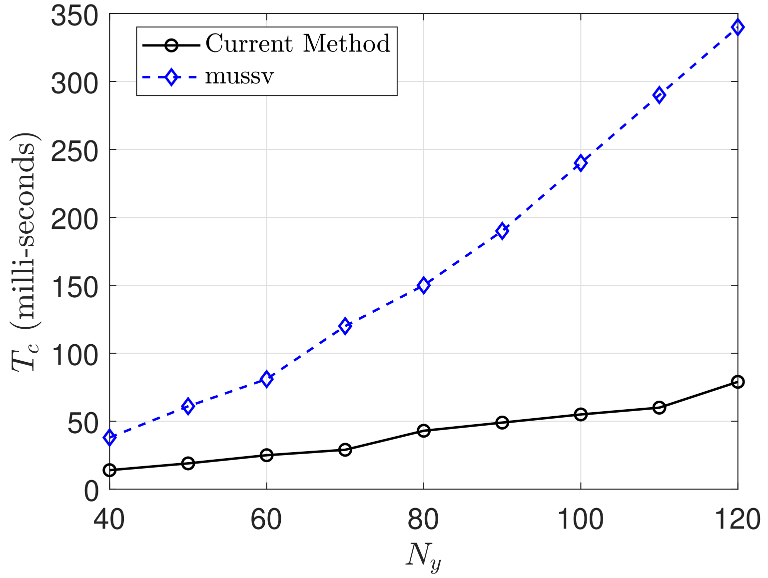

Fig. 9 The computation times for the current method (Algorithm 1) and mussv (with the 'Uf' option) as a function of the number of wall-normal grid points N_y. The results here are for the incompressible Couette flow at $Re = 358$ and $(k_x, k_z, \omega) = (0.196, 0.578, 0)$.

respectively (see Section 2.2 in [20] for details). We can compute these full-blocks using the power iteration outlined in Algorithm 1 as we did for the incompressible flows. In this paper, we consider a compressible plane Couette flow with a steady base flow to carry out these computations. Details on the base flow, discretized linear operators, and boundary conditions can be found in [20]. Algorithm 1 is then implemented at a chosen (k_x, k_z, ω) tuple to compute the structured uncertainty corresponding to $Re = 2 \times 10^5$ and $M_r = (0.5, 1, 2)$ where M_r denotes the Mach number. For the results in this section, we choose $(k_x, k_z, \omega) = (0.01, 11.24, -0.01)$ for $M_r = 0.5$, $(k_x, k_z, \omega) = (0.015, 13.78, -0.01)$ for $M_r = 1$, and $(k_x, k_z, \omega) = (0.015, 11.24, -0.01)$ for $M_r = 2$. These choices are primarily motivated by the fact

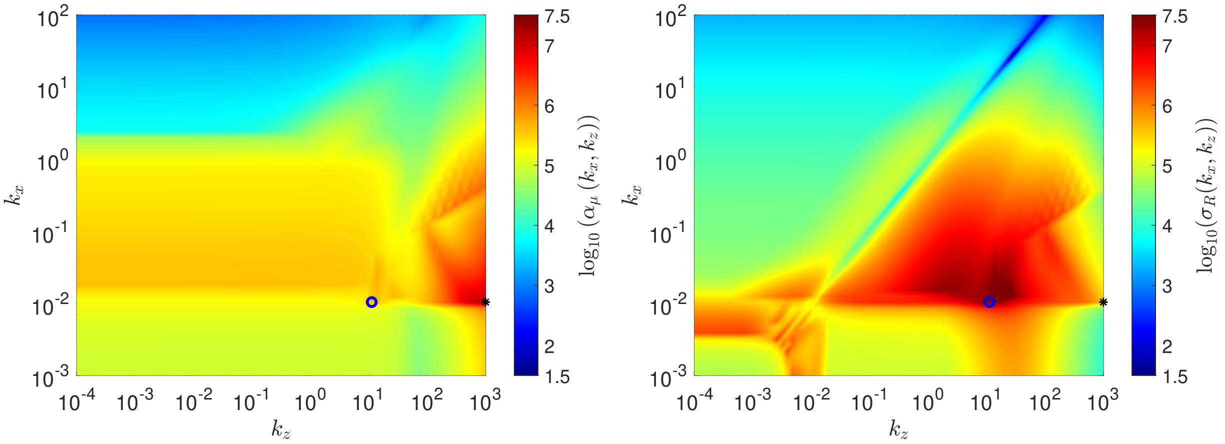

(a) μ upper bound for M_r = 0.5 **(b) Resolvent gain for M_r = 0.5**

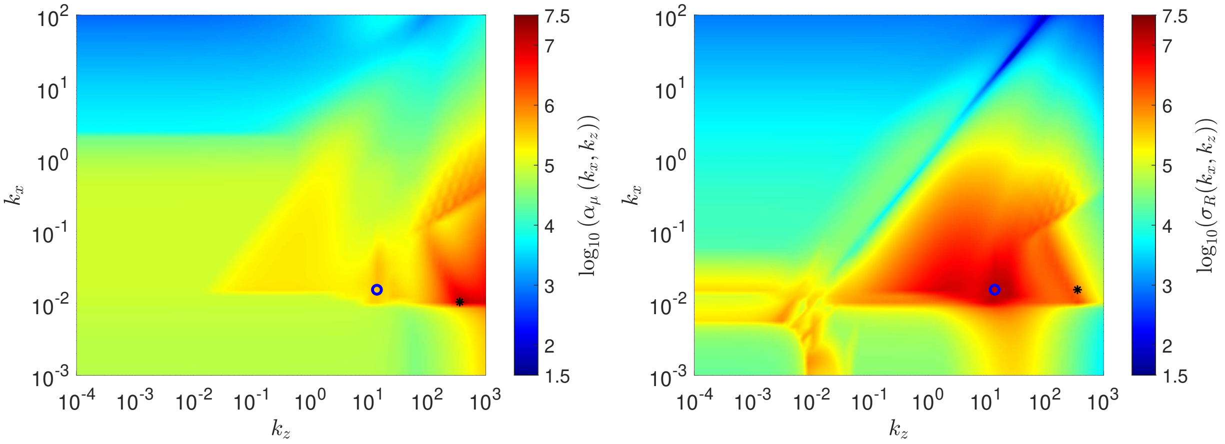

(c) μ upper bound for M_r = 1 **(d) Resolvent gain for M_r = 1**

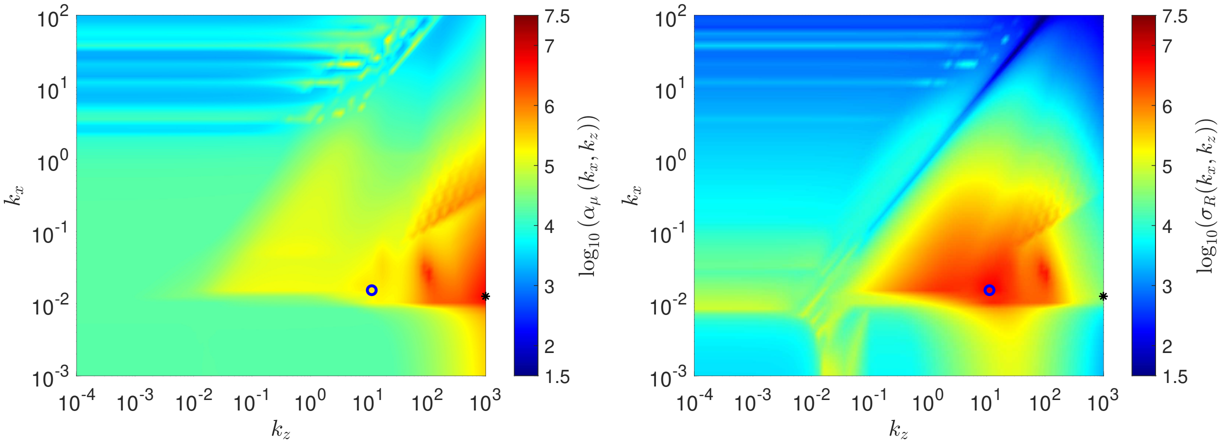

(e) μ upper bound for M_r = 2 **(f) Resolvent gain for M_r = 2**

Fig. 10 Distributions of the μ upper (log-scaled) and the resolvent gain (log-scaled) over the wavenumber pair (k_x, k_z) grid for $M_r = (0.5, 1, 2)$. The circle and the asterisk denote the (k_x, k_z) values associated with the largest computed resolvent gain and μ bounds, respectively. Note that these results are adopted here from Ref. [20].

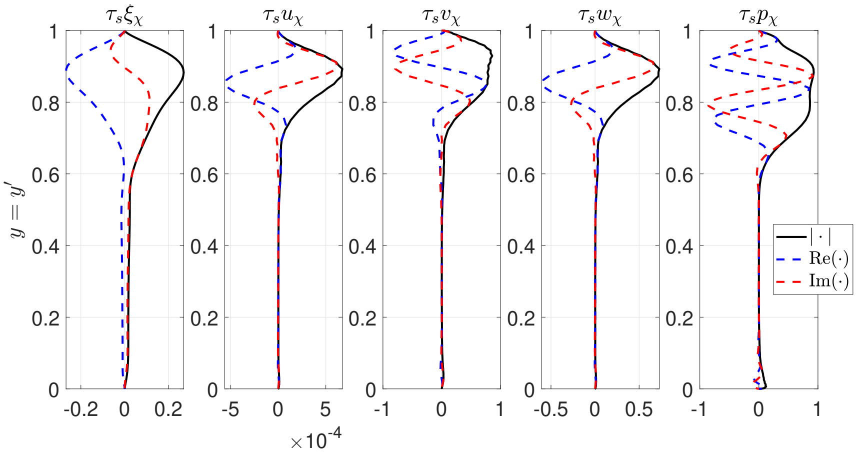

(a) $M_r = 0.5$ **(subsonic), and** $(k_x, k_z, \omega) = (0.01, 11.24, -0.01)$

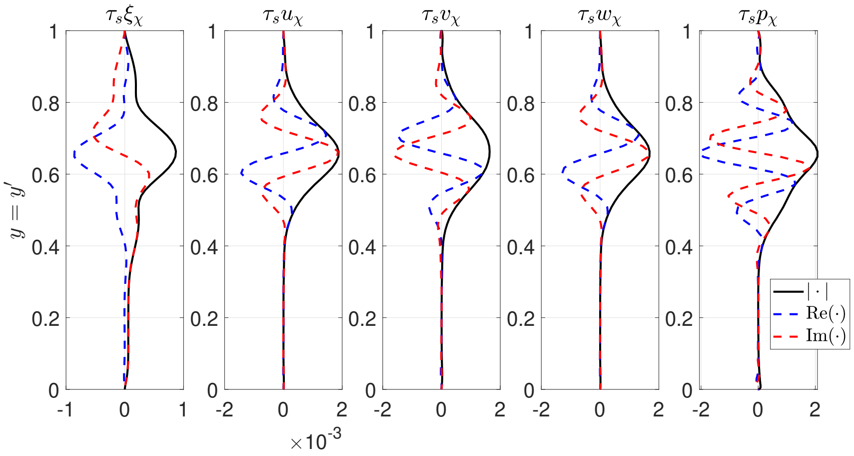

(b) $M_r = 1$ **(Transonic), and** $(k_x, k_z, \omega) = (0.015, 13.78, -0.01)$

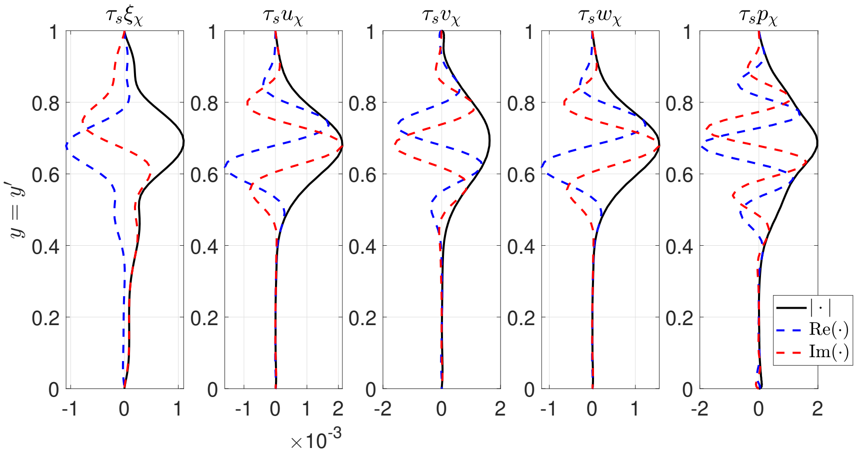

(c) $M_r = 2$ **(Supersonic) and** $(k_x, k_z, \omega) = (0.015, 11.24, -0.01)$

Fig. 11 The auto-correlation in the specific volume, velocity components and pressure as captured via the structured uncertainty for the compressible Couette flow at $Re = 2 \times 10^5$**. The parameter** τ_s **serves as a scaling factor for the purposes of illustration and here we have** $\tau_s = 10^7$**. Also, note that for** $c \in \mathbb{C}$, $|c|$, $\mathrm{Re}(c)$, **and** $\mathrm{Im}(c)$ **respectively denote the absolute value, the real part and the imaginary part of** c**.**

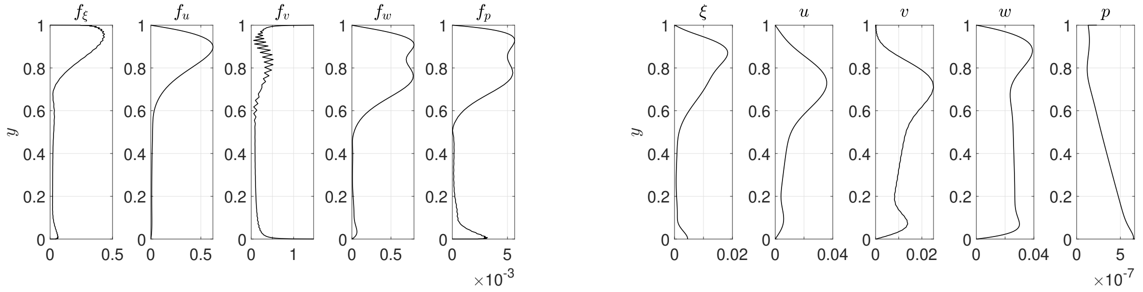

(a) Structured I/O forcing modes ($M_r = 0.5$) **(b) Structured I/O response modes ($M_r = 0.5$)**

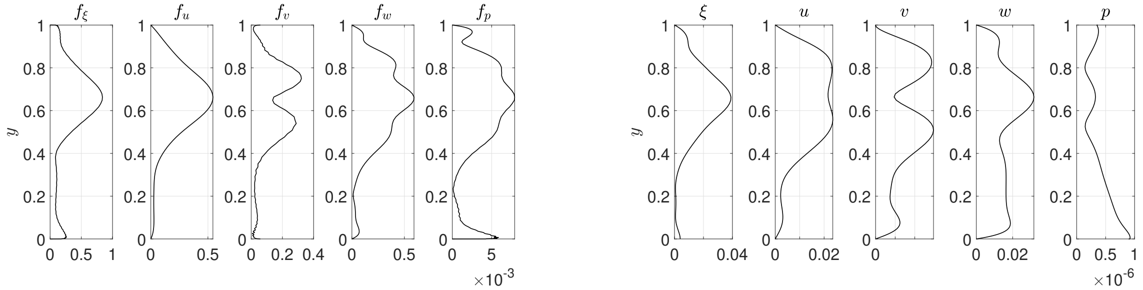

(c) Structured I/O forcing modes ($M_r = 1$) **(d) Structured I/O response modes ($M_r = 1$)**

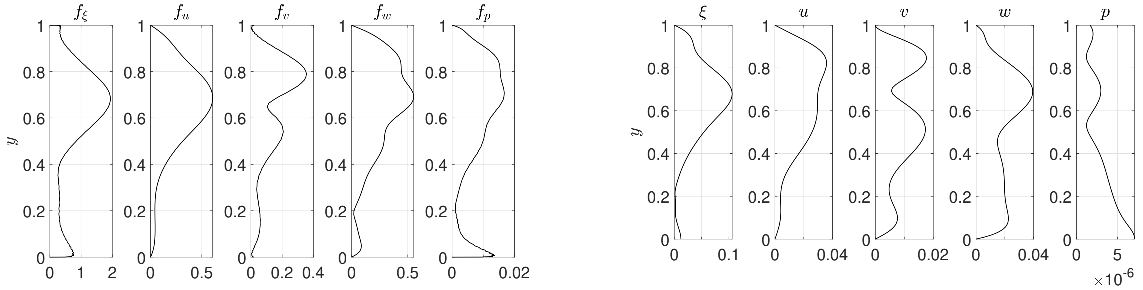

(e) Structured I/O forcing modes ($M_r = 2$) **(f) Structured I/O response modes ($M_r = 2$)**

Fig. 12 Absolute values of the structured I/O forcing and response modes for $M_r = (0.5, 1, 2)$. The (k_x, k_z, ω) tuples here corresponds to the largest resolvent gains. Note that these results are adopted here from Ref. [20].

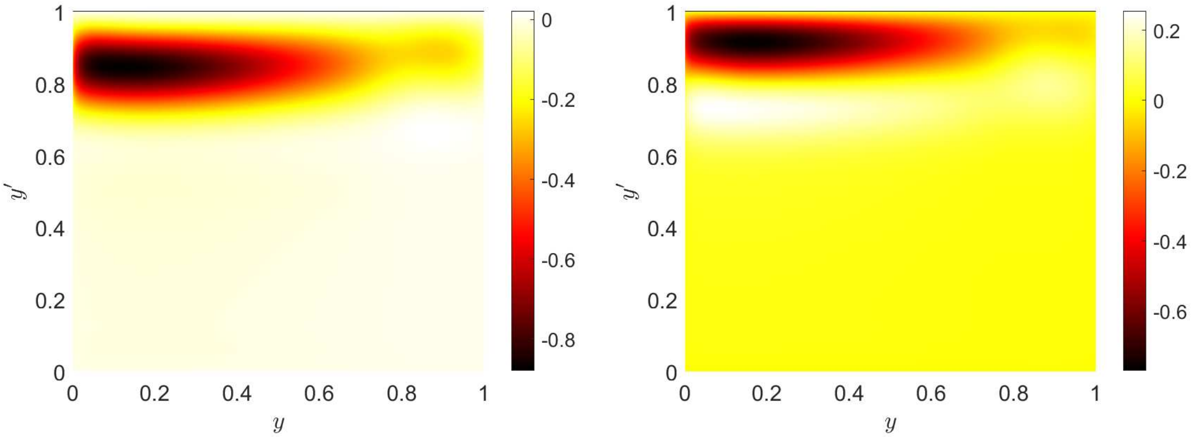

(a) $\mathrm{Re}\left(\tau_s \xi_\chi\right)$ **(b)** $\mathrm{Im}\left(\tau_s \xi_\chi\right)$

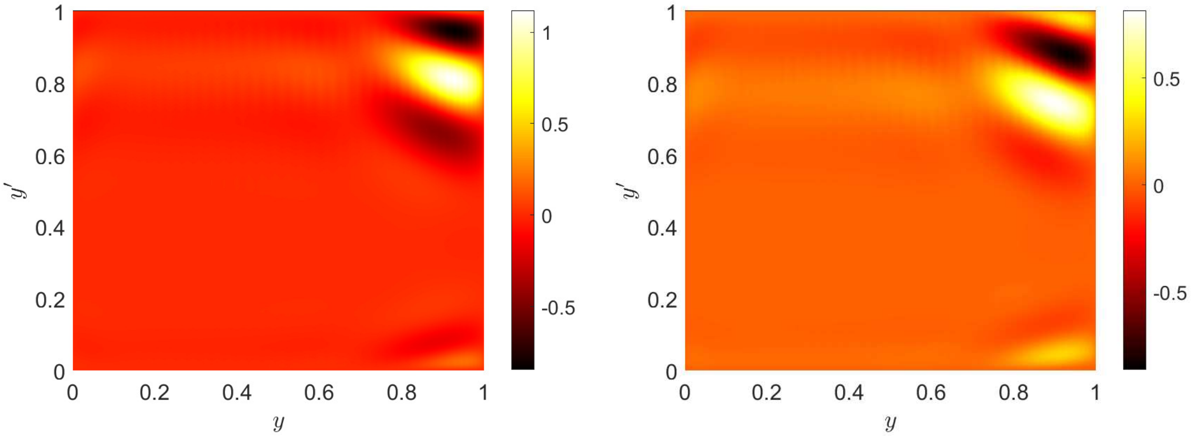

(c) $\mathrm{Re}\left(\tau_s v_\chi\right)$ **(d)** $\mathrm{Im}\left(\tau_s v_\chi\right)$

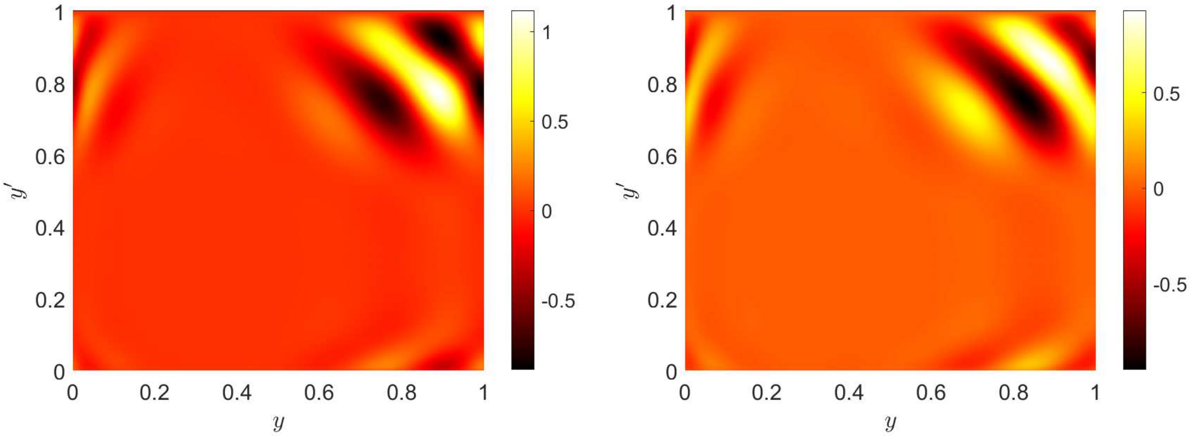

(e) $\mathrm{Re}\left(\tau_s p_\chi\right)$ **(f)** $\mathrm{Im}\left(\tau_s p_\chi\right)$

Fig. 13 Spatial correlations in the specific volume, velocity components and pressure as captured via the structured uncertainty for the compressible Couette flow at $M_r = 0.5$, $Re = 2{\times}10^5$ and $(k_x, k_z, \omega) = (0.01, 11.24, -0.01)$. The parameter τ_s serves as a scaling factor for the purposes of illustration and here we have $\tau_s = 10^7$. Also, note that for $c \in \mathbb{C}$, $\mathrm{Re}(c)$ and $\mathrm{Im}(c)$ respectively denote the real and the imaginary parts of c.

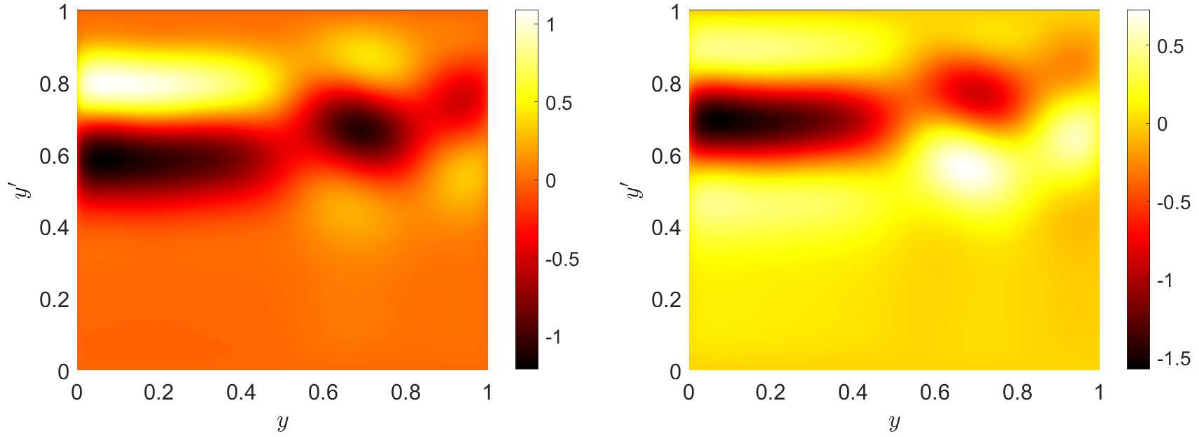

(a) Re $\left(\tau_s \xi_\chi\right)$ **(b)** Im $\left(\tau_s \xi_\chi\right)$

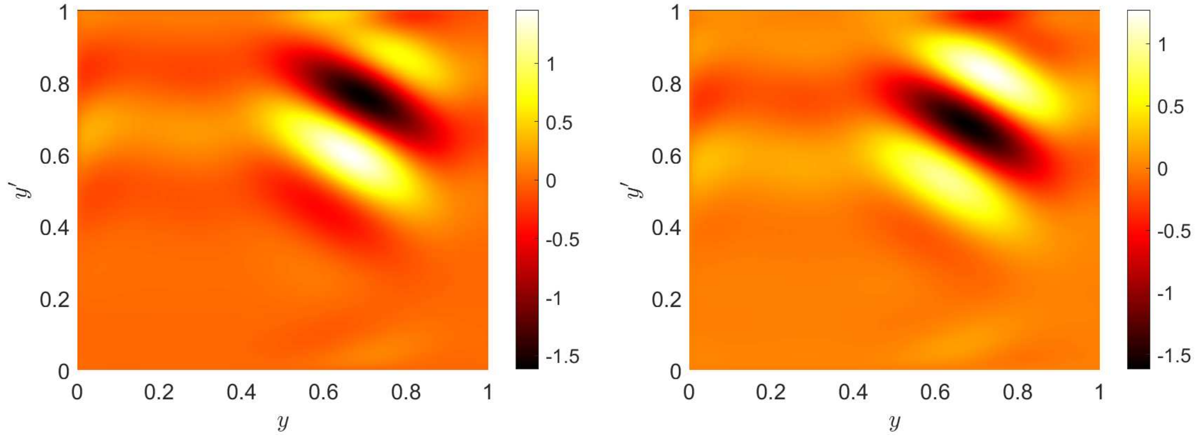

(c) Re $\left(\tau_s v_\chi\right)$ **(d)** Im $\left(\tau_s v_\chi\right)$

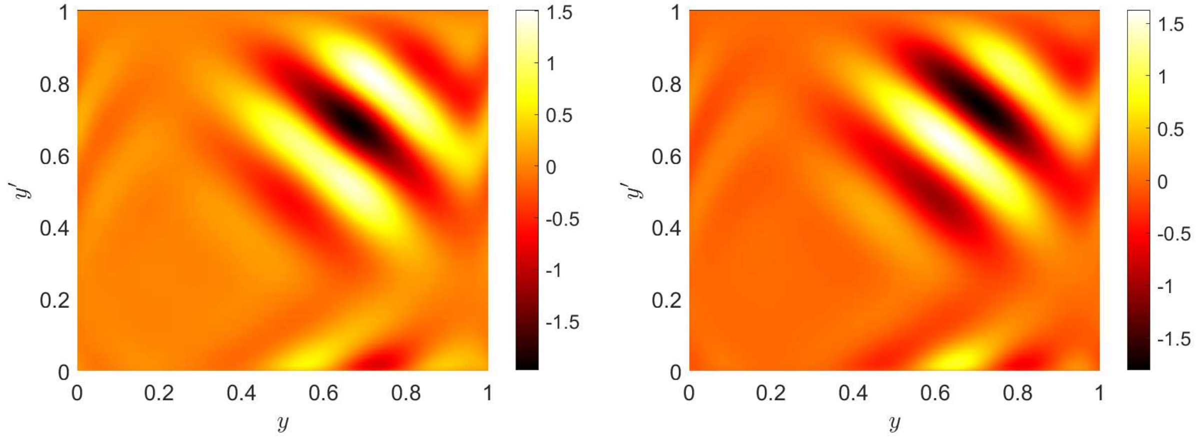

(e) Re $\left(\tau_s p_\chi\right)$ **(f)** Im $\left(\tau_s p_\chi\right)$

Fig. 14 Spatial correlations in the specific volume, velocity components and pressure as captured via the structured uncertainty for the compressible Couette flow at $M_r = 2$, $Re = 2{\times}10^5$ and $(k_x, k_z, \omega) = (0.015, 11.24, -0.01)$. The parameter τ_s serves as a scaling factor for the purposes of illustration and here we have $\tau_s = 10^7$. Also, note that for $c \in \mathbb{C}$, $\mathrm{Re}(c)$ and $\mathrm{Im}(c)$ respectively denote the real and the imaginary parts of c.

that these (k_x, k_z, ω) correspond to maxima (local or global on the wavenumber pair grid considered [20]) in both the structured I/O and resolvent gains, as shown in Fig. 10. Thus, these (k_x, k_z, ω) tuples corresponds to a potential source of instability [20]. The spatial auto-correlation structures for $M_r = 0.5$, $M_r = 1$, and $M_r = 2$ are shown respectively in Figs. 11a, 11b, and 11c. These results indicate that the auto-correlations in all the flow states are mostly concentrated near the upper wall at the subsonic Mach number but shift more towards the channel center with an increase in the Mach number. The structured I/O forcing and response modes for this instability mechanism are illustrated in Fig. 12 and the above observation is consistent with the structured I/O forcing mode shapes (see Figs. 12a, 12c, 12e). Since the structured forcing modes get mapped from the corresponding response modes via the structured uncertainty, these spatial structures likely play a key role in determining the response mode shapes.

It is interesting to note that the specific volume auto-correlations at the subsonic Mach number are relatively small in magnitude compared to the transonic and supersonic counterparts. This indicates that the instability modifies the thermodynamic properties of the base flow more as the Mach number increases. This spatial feature is in agreement with the Mach number variation of structured modal forcing of the instability. Therefore, these auto-correlation structures are connected with the modal behavior of the underlying instability mechanism. However, there are some discrepancies that have been observed as well. Especially, the dominant momentum auto-correlations are associated with the wall-normal and spanwise velocity components across the Mach number range considered here. This does not match with the conclusions drawn by analyzing the momentum forcing mode shapes for this instability (compare results in Fig. 11 and 12). A full analysis into the connections between the spatial structures and the structured I/O mode shapes is an integral part of our ongoing efforts.

The correlations in the wall-normal coordinate for $M_r = (0.5, 2)$ are shown in Figs. 13, 14. These plots capture spatially localized flow features that are potentially connected with the flow physics of the underlying instability. It is notable that these localized features get amplified as the Mach number increases. In particular, the specific volume correlations grow approximately two fold, which is consistent with the findings in terms of the auto-correlations and the forcing modes. Our current effort are focused on extracting the flow physics that are described through these localized spatial structures.

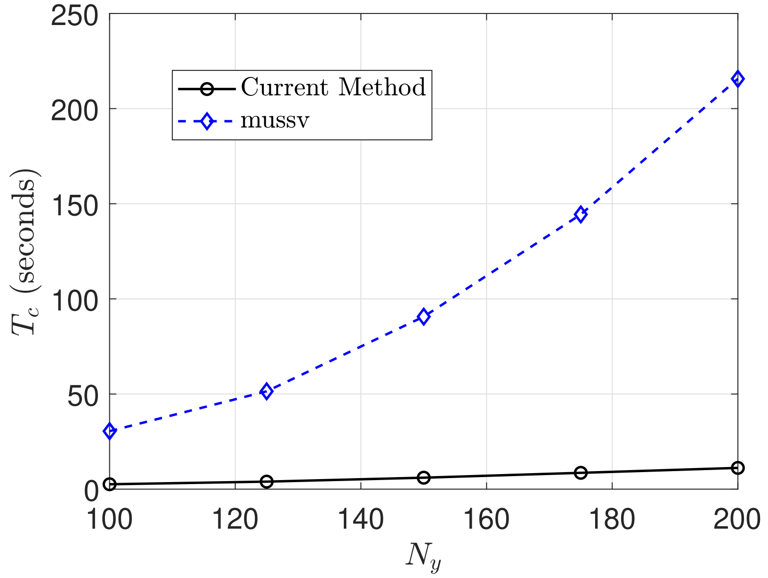

Fig. 15 The computation times for the current method (Algorithm 1) and mussv (with the 'Uf' option) as a function of the number of wall-normal grid points N_y. The results here are for the compressible, plane Couette flow at $Re = 2 \times 10^5$, $M_r = 2$ and $(k_x, k_z, \omega) = (0.015, 11.24, -0.01)$.

Similar to the incompressible flow, a comparison between computation times for the current method and mussv is carried out, and these results are illustrated in Fig. 15. Note that the overheads associated with mussv, coupled with the increased dimensionality of the operators describing the compressible flow, leads to the increased computation times here. Our implementation of Algorithm 1 shows moderate growth in computation times with an increase in the number of wall-normal grid points. This means that the current method would require fewer computational resources to carry out a structured I/O analysis of compressible flows.

V. Conclusions and Future Work

We propose a computationally efficient means of computing flow-field features that are associated with quasi-secondary instabilities in compressible flows. Results for incompressible flows are included that reconfirm recent findings in the literature through a simpler structured I/O modeling. The spatial auto-correlation structures associated with the compressible flow results are able to capture the evolution of the momentum and thermodynamic characteristics of the underlying flow instability with the Mach number. The specific volume auto-correlations amplify with Mach number and thereby introduce larger modifications to the thermodynamic properties of the base flow. These are found to be consistent with the structured forcing modes. Our current efforts are focused on characterizing quasi-secondary instabilities in compressible turbulent boundary layer flows and seeking connections with traditional secondary stability results in the existing literature.

Acknowledgments

This material is based upon work supported by the Office of Naval Research under award number N00014-22-1-2029. The authors thank Peter Seiler for technical discussions on the structured singular value.

References

[1] Jovanović, M. R., and Bamieh, B., “Componentwise energy amplification in channel flows,” *Journal of Fluid Mechanics*, Vol. 534, 2005, pp. 145–183. https://doi.org/10.1017/S0022112005004295.

[2] McKeon, B. J., and Sharma, A. S., “A critical-layer framework for turbulent pipe flow,” *Journal of Fluid Mechanics*, Vol. 658, 2010, pp. 336–382. https://doi.org/10.1017/S002211201000176X.

[3] McKeon, B., “The engine behind (wall) turbulence: perspectives on scale interactions,” *Journal of Fluid Mechanics*, Vol. 817, 2017, p. P1. https://doi.org/10.1017/jfm.2017.115.

[4] Jovanović, M. R., “From bypass transition to flow control and data-driven turbulence modeling: an input–output viewpoint,” *Annual Review of Fluid Mechanics*, Vol. 53, No. 1, 2021, pp. 311–345. https://doi.org/10.1146/annurev-fluid-010719-060244.

[5] Nichols, J. W., and Candler, G. V., “Input-output analysis of complex hypersonic boundary layers,” *AIAA SciTech 2019 Forum, AIAA Paper 2019-1383*, 2019. https://doi.org/10.2514/6.2019-1383.

[6] Dawson, S. T., and McKeon, B. J., “Studying the effects of compressibility in planar Couette flow using resolvent analysis,” *AIAA SciTech 2019 Forum, AIAA Paper 2019-2139*, 2019. https://doi.org/10.2514/6.2019-2139.

[7] Bae, H. J., Dawson, S. T., and McKeon, B. J., “Resolvent-based study of compressibility effects on supersonic turbulent boundary layers,” *Journal of Fluid Mechanics*, Vol. 883, 2020, p. A29. https://doi.org/10.1017/jfm.2019.881.

[8] Bae, H. J., Dawson, S. T., and McKeon, B. J., “Studying the effect of wall cooling in supersonic boundary layer flow using resolvent analysis,” *AIAA SciTech 2020 Forum, AIAA Paper 2020-0575*, 2020. https://doi.org/10.2514/6.2020-0575.

[9] Sun, Y., Liu, Q., Cattafesta, L. N., Ukeiley, L. S., and Taira, K., “Resolvent analysis of compressible laminar and turbulent cavity flows,” *AIAA Journal*, Vol. 58, No. 3, 2020. https://doi.org/10.2514/1.J058633.

[10] Chen, X., Cheng, C., Fu, L., and Gan, J., “Linear response analysis of supersonic turbulent channel flows with a large parameter space,” *Journal of Fluid Mechanics*, Vol. 962, 2023, p. A7. https://doi.org/10.1017/jfm.2023.244.

[11] Dwivedi, A., Sidharth, G., Nichols, J. W., Candler, G. V., and Jovanović, M. R., “Reattachment streaks in hypersonic compression ramp flow: an input–output analysis,” *Journal of Fluid Mechanics*, Vol. 880, 2019, pp. 113–135. https://doi.org/10.1017/jfm.2019.702.

[12] Dawson, S. T., and McKeon, B. J., “Prediction of resolvent mode shapes in supersonic turbulent boundary layers,” *International Journal of Heat and Fluid Flow*, Vol. 85, 2020, p. 108677. https://doi.org/10.1016/j.ijheatfluidflow.2020.108677.

[13] Liu, C., and Gayme, D. F., "Structured input–output analysis of transitional wall-bounded flows," *Journal of Fluid Mechanics*, Vol. 927, 2021. https://doi.org/10.1017/jfm.2021.762.

[14] Mushtaq, T., Bhattacharjee, D., Seiler, P., and Hemati, M. S., "Structured singular value of a repeated complex full-block uncertainty," *International Journal of Robust and Nonlinear Control*, Vol. 34, No. 7, 2024, pp. 4881–4897. https://doi.org/10.1002/rnc.7238.

[15] Mushtaq, T., Seiler, P., and Hemati, M. S., "Exact solution for the rank-one structured singular value with repeated complex full-block uncertainty," *Automatica*, Vol. 167, 2024, p. 111717. https://doi.org/10.1016/j.automatica.2024.111717.

[16] Mushtaq, T., Bhattacharjee, D., Seiler, P. J., and Hemati, M., "Structured Input-Output Tools for Modal Analysis of a Transitional Channel Flow," *AIAA SciTech 2023 Forum, AIAA Paper 2023-1805*, 2023. https://doi.org/10.2514/6.2023-1805.

[17] Liu, C., Colm-cille, P. C., and Gayme, D. F., "Structured input–output analysis of stably stratified plane Couette flow," *Journal of Fluid Mechanics*, Vol. 948, 2022, p. A10. https://doi.org/10.1017/jfm.2022.648.

[18] Mushtaq, T., Luhar, M., and Hemati, M., "Structured Input-Output Analysis of Turbulent Flows over Riblets," *AIAA AVIATION 2023 Forum, AIAA Paper 2023-3446*, 2023. https://doi.org/10.2514/6.2023-3446.

[19] Bhattacharjee, D., Mushtaq, T., Seiler, P. J., and Hemati, M. S., "Structured input-output analysis of compressible plane Couette flow," *AIAA SciTech 2023 Forum, AIAA Paper 2023-1984*, 2023. https://doi.org/10.2514/6.2023-1984.

[20] Bhattacharjee, D., Mushtaq, T., Seiler, P., and Hemati, M. S., "Structured Input-Output Modeling and Robust Stability Analysis of Compressible Flows," *arXiv preprint arXiv:2407.14986*, 2024. https://doi.org/10.48550/arXiv.2407.14986.

[21] Liu, C., and Gayme, D. F., "Input-output inspired method for permissible perturbation amplitude of transitional wall-bounded shear flows," *Phys. Rev. E*, Vol. 102, 2020, p. 063108. https://doi.org/10.1103/PhysRevE.102.063108.

[22] Liu, C., Shuai, Y., Rath, A., and Gayme, D. F., "A structured input-output approach to characterizing optimal perturbations in wall-bounded shear flows," *2023 American Control Conference (ACC)*, 2023, pp. 2319–2325. https://doi.org/10.23919/ACC55779.2023.10156058.

[23] Orszag, S. A., and Patera, A. T., "Secondary instability of wall-bounded shear flows," *Journal of Fluid Mechanics*, Vol. 128, 1983, pp. 347–385. https://doi.org/10.1017/S0022112083000518.

[24] Herbert, T., "Secondary instability of boundary layers," *Annual review of fluid mechanics*, Vol. 20, 1988, pp. 487–526. https://doi.org/10.1146/annurev.fl.20.010188.002415.

[25] Schmid, P. J., and Henningson, D. S., *Stability and Transition in Shear Flows: Applied Mathematical Sciences*, Springer New York, NY, 2002.

[26] Jouin, A., Ciola, N., Cherubini, S., and Robinet, J. C., "Detuned secondary instabilities in three-dimensional boundary-layer flow," *Physical Review Fluids*, Vol. 9, No. 4, 2024, p. 043901. https://doi.org/10.1103/PhysRevFluids.9.043901.

[27] Shuai, Y., Liu, C., and Gayme, D. F., "Structured input–output analysis of oblique laminar–turbulent patterns in plane Couette–Poiseuille flow," *International Journal of Heat and Fluid Flow*, Vol. 103, 2023, p. 109207. https://doi.org/10.1016/j.ijheatfluidflow.2023.109207.

[28] Balas, G., Chiang, R., Packard, A., and Safonov, M., "Robust control toolbox user's guide," *The Math Works, Inc., Tech. Rep*, 2007.

[29] Kerswell, R., "Nonlinear Nonmodal Stability Theory," *Annual Review of Fluid Mechanics*, Vol. 50, No. 1, 2018, pp. 319–345. https://doi.org/10.1146/annurev-fluid-122316-045042.

[30] Kalur, A., Seiler, P., and Hemati, M. S., "Stability and performance analysis of nonlinear and non-normal systems using quadratic constraints," *AIAA Aerospace Sciences Meeting, AIAA Paper 2020-0833*, 2020. https://doi.org/10.2514/6.2020-0833.

[31] Kalur, A., Seiler, P., and Hemati, M. S., "Nonlinear stability analysis of transitional flows using quadratic constraints," *Physical Review Fluids*, Vol. 6, No. 4, 2021, p. 044401. https://doi.org/10.1103/PhysRevFluids.6.044401.

[32] Kalur, A., Mushtaq, T., Seiler, P., and Hemati, M. S., "Estimating regions of attraction for transitional flows using quadratic constraints," *IEEE Control Systems Letters*, Vol. 6, 2021, pp. 482–487. https://doi.org/10.1109/LCSYS.2021.3081382.

[33] Goulart, P. J., and Chernyshenko, S., "Global stability analysis of fluid flows using sum-of-squares," *Physica D: Nonlinear Phenomena*, Vol. 241, No. 6, 2012, pp. 692–704. https://doi.org/10.1016/j.physd.2011.12.008.

[34] Packard, A., and Doyle, J., "The complex structured singular value," *Automatica*, Vol. 29, No. 1, 1993, pp. 71–109. https://doi.org/10.1016/0005-1098(93)90175-S.

[35] Zhou, K., Doyle, J., and Glover, K., *Robust and Optimal Control*, Prentice Hall, 1996.

[36] Braatz, R. P., Young, P. M., Doyle, J. C., and Morari, M., "Computational complexity of μ calculation," *IEEE Transactions on Automatic Control*, Vol. 39, No. 5, 1994, pp. 1000–1002. https://doi.org/10.1109/9.284879.

[37] Poljak, S., and Rohn, J., "Checking robust nonsingularity is NP-hard," *Mathematics of Control, Signals and Systems*, Vol. 6, No. 1, 1993, pp. 1–9. https://doi.org/10.1007/BF01213466.

[38] Coxson, G. E., and DeMarco, C. L., "The computational complexity of approximating the minimal perturbation scaling to achieve instability in an interval matrix," *Mathematics of Control, Signals and Systems*, Vol. 7, No. 4, 1994, pp. 279–291. https://doi.org/10.1007/BF01211520.

[39] Packard, A., Fan, M., and Doyle, J., "A power method for the structured singular value," *Proceedings of the 27th IEEE Conference on Decision and Control*, IEEE, 1988, pp. 2132–2137. https://doi.org/10.1109/CDC.1988.194710.